



Cite this: *Nanoscale*, 2024, **16**, 657

Novel hollow $\text{MoS}_2@\text{C}@\text{Cu}_2\text{S}$ heterostructures for high zinc storage performance†

Yujin Li,^{a,c} Jing Xu,^{*a} Xinqi Luo,^a Futing Wang,^c Zhong Dong,^a Ke-Jing Huang,^{ID *b} Chengjie Hu,^a Mengyi Hou^a and Ren Cai ^{ID *c}

Heterostructured materials have great potential as cathodes for zinc-ion batteries (ZIBs) because of their fast Zn^{2+} transport channels. Herein, hollow $\text{MoS}_2@\text{C}@\text{Cu}_2\text{S}$ heterostructures are innovatively constructed using a template-engaged method. The carbon layer improves the electrical conductivity, provides a high *in situ* growth area, and effectively restricts volume expansion during the recycling process. MoS_2 nanosheets are grown on the surfaces of hollow $\text{C}@\text{Cu}_2\text{S}$ nanocubes using the *in situ* template method, further expanding the specific surface area and exposing more active sites to enhance the electrical conductivity. As expected, an admirable reversible capacity of $197.2 \text{ mA h g}^{-1}$ can be maintained after 1000 cycles with a coulombic efficiency of 91.1%. Therefore, we firmly believe that this work points the way forward for high-performance materials design and energy storage systems.

Received 17th October 2023,
Accepted 17th November 2023

DOI: 10.1039/d3nr05231a
rsc.li/nanoscale

^aCollege of Chemistry and Chemical Engineering, Xinyang Normal University, Xinyang 464000, China

^bEducation Department of Guangxi Zhuang Autonomous Region, Key Laboratory of Applied Analytical Chemistry, Guangxi Collaborative Innovation Center for Chemistry and Engineering of Forest Products, Guangxi Key Laboratory of Chemistry and Engineering of Forest Products, Key Laboratory of Chemistry and Engineering of Forest Products, State Ethnic Affairs Commission, School of Chemistry and Chemical Engineering, Guangxi Minzu University, Nanning 530006, China

^cMolecular Science and Biomedicine Laboratory, State Key Laboratory for Chemo/Bio-Sensing and Chemometrics, College of Material Science and Engineering, College of Chemistry and Chemical Engineering, College of Biology, Hunan University, Changsha, 410082, China

† Electronic supplementary information (ESI) available. See DOI: <https://doi.org/10.1039/d3nr05231a>



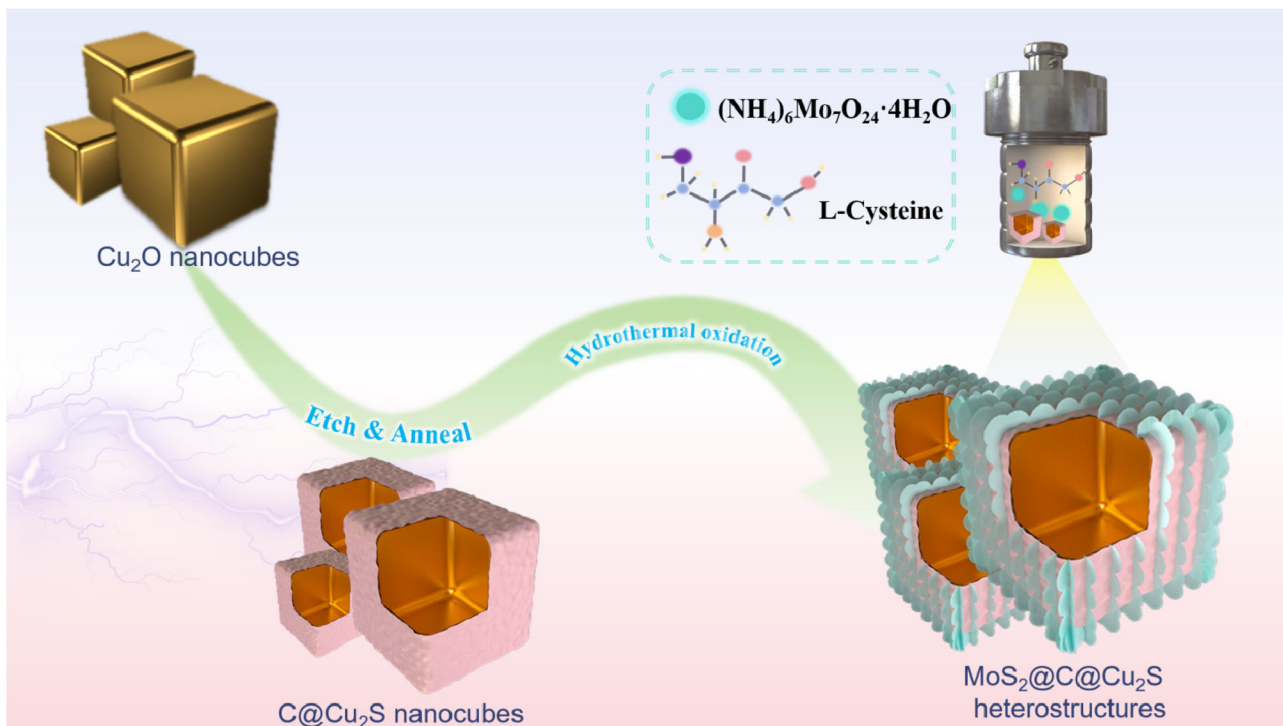
Ren Cai

the young editorial board of *Collagen and Leather and Exploration*, respectively.

Introduction

With the development of advanced energy storage technologies, lithium-ion batteries (LIBs) have exhibited some inevitable defects, such as high cost and potential safety hazards.^{1–3} Currently, aqueous system zinc ion batteries (ZIBs) are expected to be alternatives to LIBs due to their low cost, abundant resources, and high security.^{4,5} Although there have been many advances in the research on ZIBs, the design of high-performance ZIBs still faces great challenges, such as slow diffusion of zinc ions and low reversibility, which seriously hinder their development and commercialization.^{6,7}

As a new type of 2D structure, many transition metal dichalcogenides (TMDs) are attracting attention as novel energy storage materials, because of their efficient energy conversion.^{8–11} For example, $\text{VS}_4@\text{rGO}$ nanosheets were explored using a hydrothermal process for super-performance ZIBs;¹² as a novel electrode, WS_2 nanosheets exhibited high specific capacity and were applied in sodium-ion batteries;¹³ $\text{SnS}_2/\text{Ti}_3\text{C}_2\text{T}_x$ nanosheets were fabricated using an *in situ* hybridization method for high-performance potassium-ion batteries.¹⁴ More interestingly, CuS nanocubes exhibited high energy density when used as cathode materials,¹⁵ and MoS_2 nanosheets are conducive to ion intercalation/deintercalation in lithium/sodium-ion batteries.^{16,17} However, there are some challenges in the application of MoS_2 nanosheets in ZIBs, such as poor conductivity, higher hydrophilicity, agglomeration, and volume expansion.^{18–20} Therefore, it is important to explore novel MoS_2 structures with high conductivity and cycling stability for energy storage.



Scheme 1 Synthetic process of the hollow MoS_2 @C@ Cu_2S heterostructures.

Herein, we fabricated novel MoS_2 @C@ Cu_2S heterostructures using a template-engaged process for high-capacity Zn^{2+} storage (Scheme 1). These heterostructures are composed of MoS_2 nanosheets and hollow $\text{C}@\text{Cu}_2\text{S}$ nanocubes, and exhibit high specific surface area, exposing many active sites and enhancing the electrical conductivity in ZIBs. The hollow cavity facilitates rapid Zn^{2+} transport to reduce the energy barrier of Zn^{2+} absorption and transport, and reinforces the volume elasticity to accommodate volume change during Zn^{2+} de-/intercalation. At current densities of 0.1 A g^{-1} and 1.0 A g^{-1} , the as-designed ZIBs exhibit stable specific capacities of $679.1 \text{ mA h g}^{-1}$ and $192.9 \text{ mA h g}^{-1}$, respectively.

Results and discussion

The hollow MoS_2 @C@ Cu_2S heterostructures (size of $\sim 600 \text{ nm}$) were prepared using an etching process followed by hydrothermal reduction (Scheme 1 and Fig. 1a and b). First, hollow CuS nanocubes with uniform sizes (size of $\sim 500 \text{ nm}$, Fig. S1b†) were prepared by the reaction of Cu_2O nanocubes (size of $\sim 550 \text{ nm}$, Fig. S1a†), Na_2S , and HCl . After carbonization, $\text{PDA}@\text{CuS}$ nanocubes converted into hollow $\text{C}@\text{Cu}_2\text{S}$ nanocubes (size of $\sim 550 \text{ nm}$, Fig. S1c†). Finally, hollow heterostructures were prepared after folding MoS_2 nanosheets were grown on the surface of hollow $\text{C}@\text{Cu}_2\text{S}$ nanocubes (Fig. 1c).

The X-ray powder diffraction (XRD) pattern shows that all peaks of the crystal phases are indexed to MoS_2 (JCPDS: 37-1492) and Cu_2S (JCPDS: 72-2276) (Fig. S2†). As exemplified in elemental distribution scanning (Fig. 1e), the distribution of C can be seen in the intermediate layer (Fig. S3†). These hollow CuS nanocubes with folding MoS_2 nanosheets and the C layer are MoS_2 @C@ Cu_2S heterostructures. As further evidence, the lattice diffraction fringe at 0.606 nm corresponds to the $(0\ 0\ 2)$ crystal plane of MoS_2 , and the fringe at 0.260 nm corresponds to the $(1\ 0\ 3)$ crystal plane of Cu_2S in the high-resolution TEM image (Fig. 1d). X-ray photoelectron spectroscopy (XPS) further confirmed that the hollow heterostructure is composed of S, Mo, C, and Cu (Fig. S3†). The $\text{E}^{1\text{g}}_{2\text{g}}$ and $\text{A}_{1\text{g}}$ peaks from MoS_2 , the Cu–S vibration, and the D-band (defect vibration) and the G-band (graphitic carbon vibration) from C are observed in Raman spectroscopy (Fig. S4†), demonstrating the presence of MoS_2 , CuS and the carbon layer in the heterostructures. In addition, the heterostructures show typical meso-shell structures with a large specific surface area of $34.10 \text{ m}^2 \text{ g}^{-1}$ (Fig. S5†).

The electrochemical properties of the MoS_2 @C@ Cu_2S heterostructures were investigated as shown in Fig. 2. As shown in Fig. 2a, the irreversible cathodic peaks at 0.32 V result from multiple electrochemical reactions, which involve the insertion of Zn^{2+} to form $\text{Zn}_x\text{Cu}_2\text{S}/\text{Zn}_x\text{MoS}_2$ and to generate ZnS and Mo. In the subsequent positive scan, the peak at 0.71 V corresponds to the dezincing of ZnS to re-generate Cu_2S and MoS_2 . Due to the formation of a solid electrolyte layer (SEI) film during the initial activation process, the loss of irre-

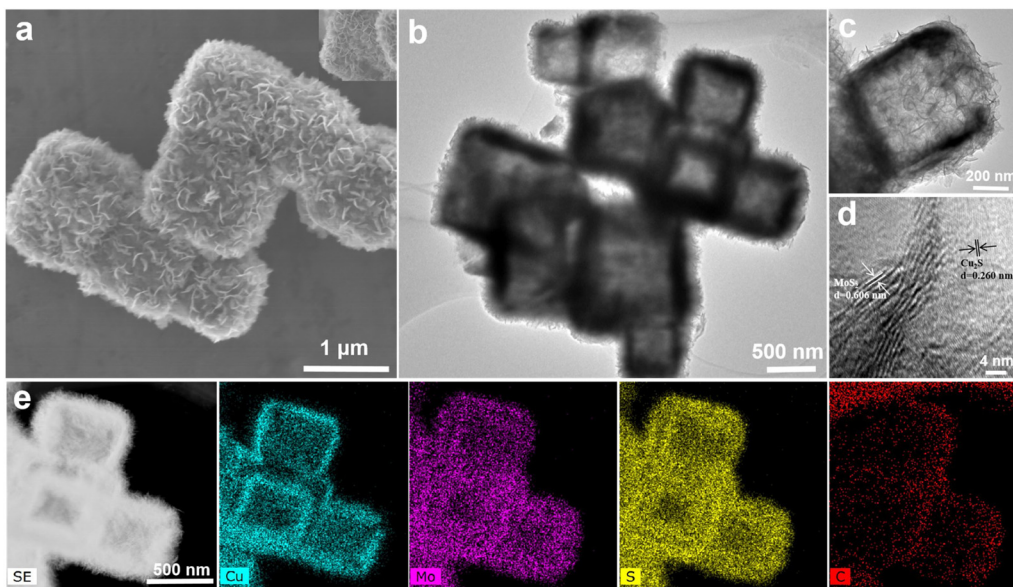


Fig. 1 Characterization of $\text{MoS}_2@\text{C}@\text{Cu}_2\text{S}$ heterostructures: (a) SEM image; (b–d) TEM images; (e) elemental mapping images.

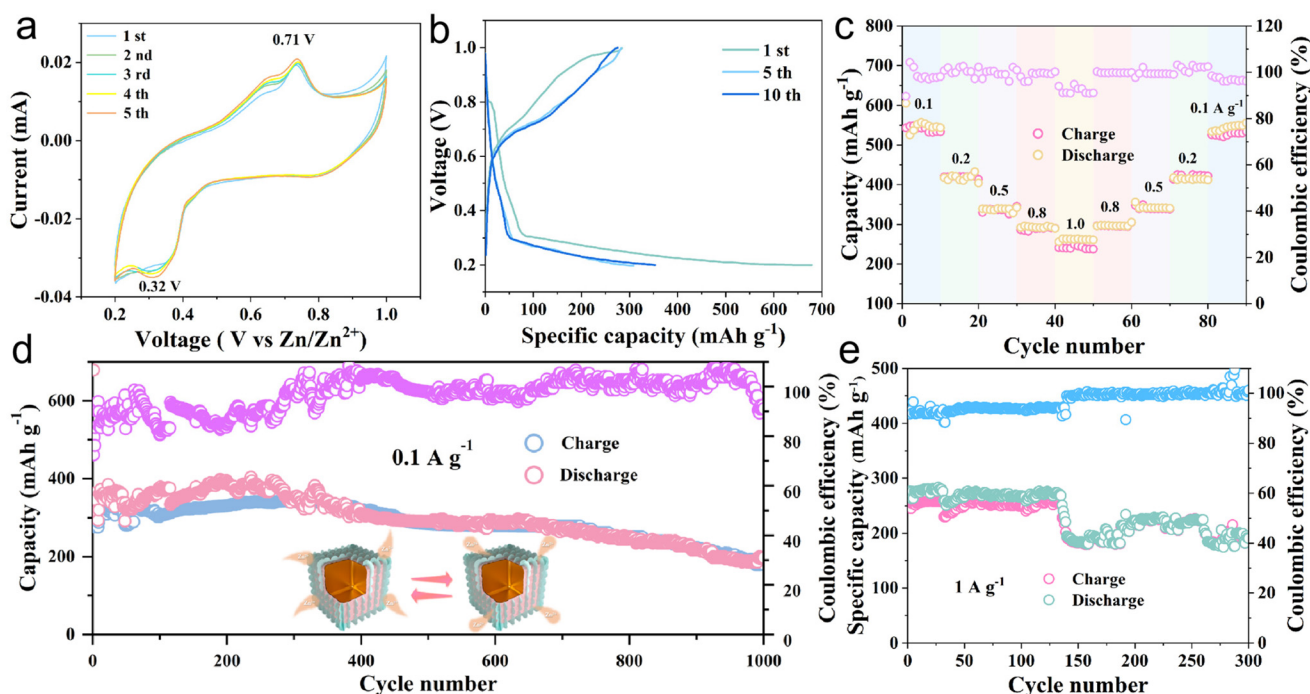


Fig. 2 The electrochemical performance tests of $\text{MoS}_2@\text{C}@\text{Cu}_2\text{S}$ heterostructures: (a) CV profiles at 0.1 mV s^{-1} ; (b) charge–discharge curves of the first, fifth, and tenth cycles; (c) rate performance; (d) long-term cycling performance; (e) high current density performance.

versible capacity results in a larger area in the initial cycle than that in the following cycles. From the second cycle to the fifth cycle, the curves show good overlap, indicating good cycling stability.

In Fig. 2b, the galvanostatic charge–discharge (GCD) test exhibits the charge–discharge curves of the heterostructures at a current density of 0.1 A g^{-1} . The charge and discharge curves

of the first, fifth, and tenth cycles show a high degree of similarity, indicating good cycling stability. For the insertion of Zn^{2+} , the voltage platforms are formed in the discharge process at 0.32 V . At 0.71 V , the platform is in the charging state, corresponding to the dezincing process. These results indicate good agreement between the GCD test and the CV curve (Fig. 2a and b). At different current densities of $0.1, 0.2,$

0.5, 0.8, 1.0, 0.8, 0.5, 0.2, and 0.1 A g⁻¹, the corresponding specific discharge capacities are 548.6, 420.2, 345.2, 292.2, 248.9, 304.8, 349.1, 424.3, and 534.1 mA h g⁻¹, respectively (Fig. 2c).

The specific capacities of the heterostructures regularly decrease with increasing current density. In contrast, when the current density decreases, the specific capacity increases, proving the excellent rate performance. Fig. 2d shows the cycling performance and the corresponding coulombic efficiency of the heterostructures after 1000 cycles at 0.1 A g⁻¹. The initial specific capacity is 679.1 mA h g⁻¹, and the specific capacities during the first few cycles are gradually enhanced, which is related to the activation of the heterostructures.²² After 1000 cycles, the specific capacity is 197.2 mA h g⁻¹ and the coulombic efficiency is 91.1%. Furthermore, at a high

current density, *i.e.*, 1 A g⁻¹, the specific capacity is 192.9 mA h g⁻¹ after 300 cycles. These results confirm that the MoS₂@C@Cu₂S heterostructures have excellent cycling stability for ZIBs at high current density. In order to investigate the reaction mechanism of Zn²⁺, the electrochemical characteristics of MoS₂@C@Cu₂S heterostructures in an aqueous electrolyte were studied using CV in the potential range of 0.2–1.0 V (vs. Zn²⁺/Zn). In Fig. 3a, a pair of redox peaks at 0.25/0.75 V is observed, representing the reversible de-intercalation process of Zn²⁺ in MoS₂ nanosheets. There is no change in the shape of the CV curves when the scanning rate increases from 0.1 to 1.0 mV s⁻¹, which indicates that the heterostructures possess good electrochemical reversibility. With an increased scan rate, the anodic peak moves to a high potential (*i.e.*, 0.76 V) from 0.72 V, and the cathodic peak shifts to a low potential

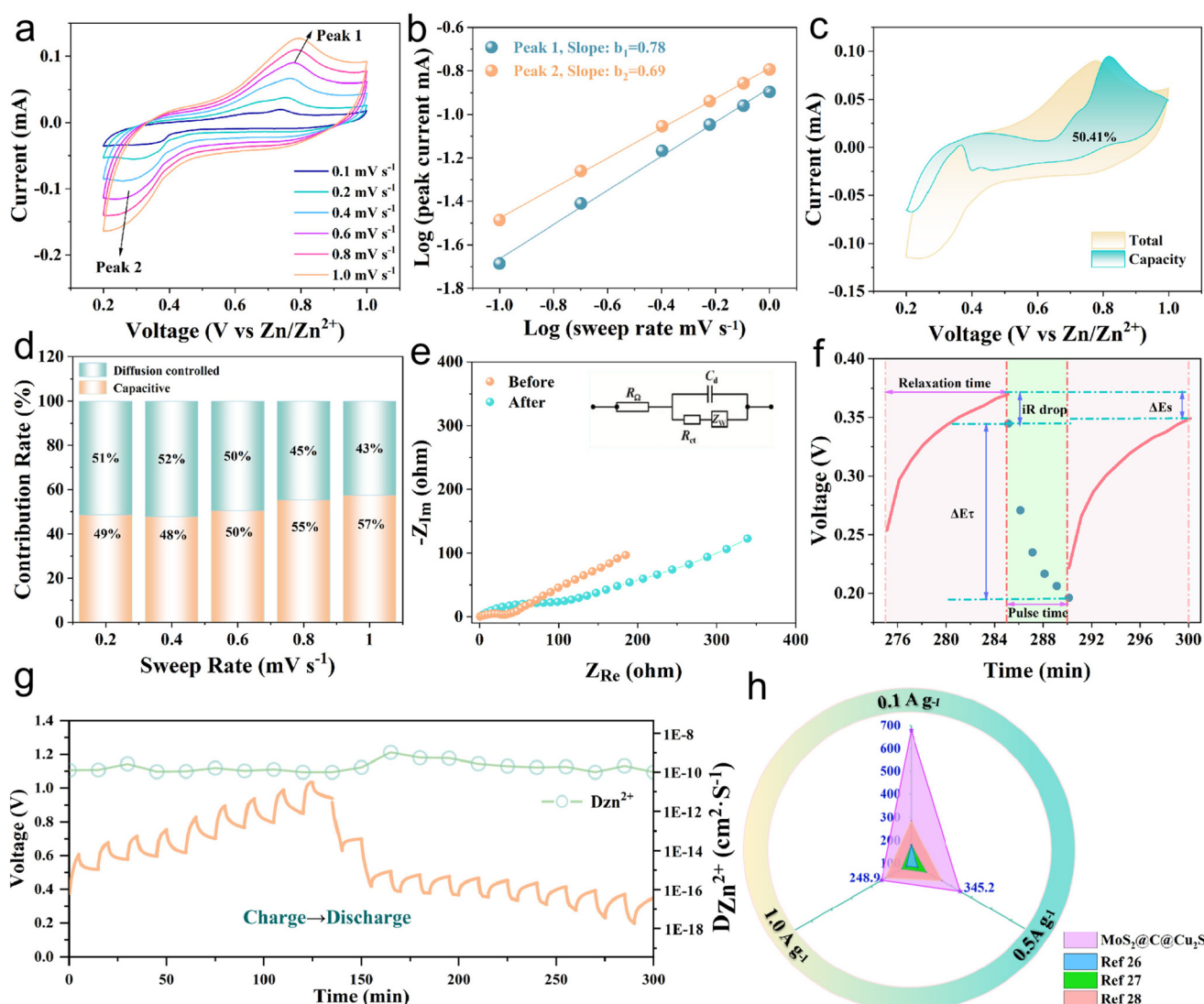


Fig. 3 (a) CV profiles at different scan rates; (b) plot of log (sweep rate) versus log (peak current) for anodic and cathodic peaks; (c) the capacitive contribution to the total capacity at 0.6 mV s⁻¹; (d) capacity contribution at different scan rates; (e) EIS plots of MoS₂@C@Cu₂S heterostructures before and after 100 cycles; (f) GITT test conditions for the heterostructures during the discharge process; (g) GITT profiles and the calculated $D_{Zn^{2+}}$ values; (h) comparison of the rate performance with those of previously reported MoS₂-based electrode materials applied in ZIBs.

(i.e., 0.25 V) from 0.38 V. These potential changes are related to the enhanced diffusion resistance.

The electrochemical kinetics of the reduction of Zn^{2+} are presented in Fig. 3b. The power formula shows that $I = a\nu^b$, $\log(I) = \log(a) + b\log(\nu)$, where I is the current, ν is the scanning rate, and a and b are adjustable parameters. The coefficient b represents the type of electrochemical charge storage. When b is in the range of 0.5 to 1, the capacitance controls the process of charge storage.²¹ Here, b was calculated to be 0.78 and 0.69 for the oxidation peak and the reduction peak, respectively, indicating that the Zn^{2+} storage process is controlled by a synergistic mechanism between the capacitive contribution and the diffusion process. The contributions of the capacitive effect ($k_1\nu$) and diffusion effect ($k_2\nu^{1/2}$) were further calculated according to the formula: $i = k_1\nu + k_2\nu^{1/2}$. The contribution ratio of the capacitance to the diffusion capacity of the heterostructures was calculated to be $\sim 50.41\%$ at a scan rate of 0.6 mV s^{-1} (Fig. 3c). In Fig. 3d, with the increasing scan rate, i.e., 0.2 to 1.0 mV s^{-1} , the capacitance contribution

is enhanced from 49% to 57%, indicating that a capacitive-controlled process dominates the storage behavior to promote the rate performance and capacity performance of ZIBs.

Next, electrochemical impedance spectroscopy (EIS) and galvanostatic intermittent titration technique (GITT) tests were executed to evaluate the kinetics of the electrode reaction in detail (Fig. 3e and f). There is a small semicircle diameter in the EIS curves of $MoS_2@C@Cu_2S$ heterostructures before and after the cycle (Fig. 3e), indicating that the heterostructures possess good electrical conductivity and rapid Zn^{2+} kinetic diffusion. Based on Fick's second law, the difference in Zn^{2+} diffusion kinetics is explored as follows:

$$D_{Zn^{2+}} = \frac{4}{\tau\pi} \left(\frac{m_B V_M}{SM_B} \right)^2 \left(\frac{\Delta E_S}{\Delta E_\tau} \right)^2$$

where τ , m_B , M_B , V_M , and S stand for the current pulse time (s), the mass, the molar mass, the molar volume of active

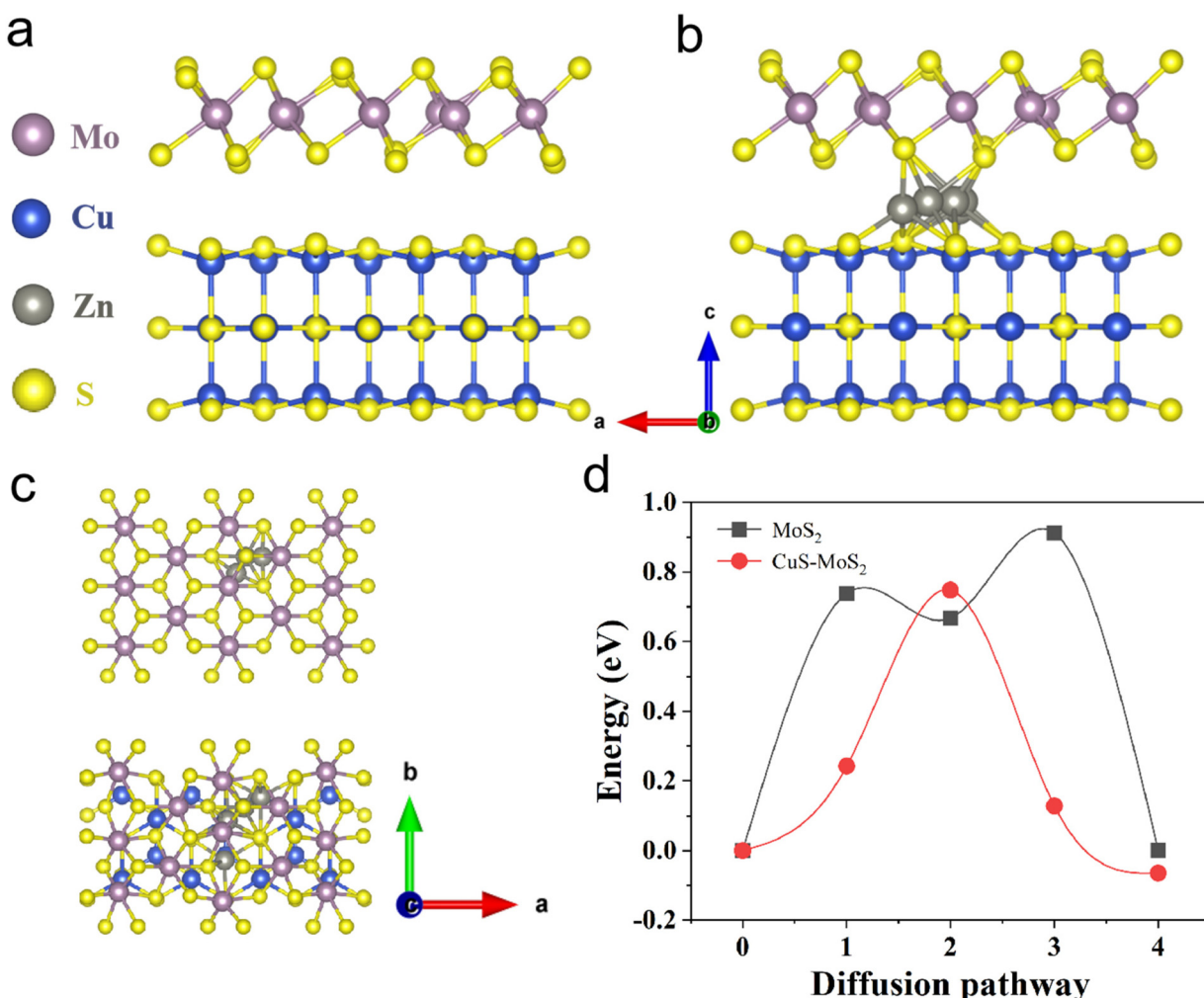


Fig. 4 (a) Optimized structure of $MoS_2@C@Cu_2S$; (b) optimized structure of Zn^{2+} insertion in $MoS_2@C@Cu_2S$; (c) top view of the optimized structure of Zn^{2+} insertion in pure MoS_2 and $MoS_2@C@Cu_2S$; (d) energy barriers of diffusion behavior of Zn^{2+} in pure MoS_2 and $MoS_2@C@Cu_2S$.

materials, and the area of the electrode, respectively;²³ the calculation method of ΔE_s and ΔE_t is also displayed in Fig. 3f. It is clearly seen that the pulse time is 5 min, the relaxation time is 10 min, and the quasi-open circuit voltage is reached, and by calculation the $D_{Zn^{2+}}$ was obtained in the range from 10^{-8} to $10^{-10} \text{ cm}^2 \text{ s}^{-1}$ (Fig. 3g), indicating that the electrode possesses good reaction kinetics.^{24,25} Compared with previous reports on MoS₂-based zinc-ion batteries (Fig. 3h),²⁶⁻²⁸ MoS₂@C@Cu₂S heterostructures exhibit high performance for ZIBs at different current densities. The excellent electrochemical characteristics of the heterostructures are closely related to the following factors: (1) ultra-thin MoS₂ nanosheets cover the surface of hollow C@Cu₂S nanocubes, which would promote fast ion transport and effectively alleviate the volume expansion;²⁹ (2) the hollow cavity, the high specific surface area (*i.e.*, $34.10 \text{ m}^2 \text{ g}^{-1}$), and a large number of electrochemical active sites would shorten the ion diffusion path;^{19,25,30} (3) the intermediate C layers maintain the stability of the heterostructures.²⁶ All three factors enable MoS₂@C@Cu₂S heterostructures to achieve superior reversible cycling performance. Density functional theory (DFT) calculations were used to analyze the diffusion of Zn²⁺ inserted in the lattice of MoS₂@C@Cu₂S heterostructures at different energy barriers. Fig. 4a exhibits the theoretical laminated structure, and Fig. 4b shows the heterostructure of the inter-layer model of Zn²⁺ insertion. Moreover, compared with the Zn²⁺ diffusion barriers of pure MoS₂ (Fig. 4c and d), the inter-layer diffusion energy barrier of Zn²⁺ decreases in MoS₂@C@Cu₂S heterostructures after MoS₂ nanosheets grow on the surface of hollow C@Cu₂S nanocubes, which further indicates that the heterostructures are conducive to Zn²⁺ diffusion.

Conclusions

In summary, novel hollow MoS₂@C@Cu₂S heterostructures were fabricated using a template-engaged process for Zn²⁺ storage. These heterostructures with sizes of $\sim 600 \text{ nm}$ are packed by folding MoS₂ nanosheets and hollow C@Cu₂S nanocubes. Because of the high surface area, *i.e.*, $34.10 \text{ m}^2 \text{ g}^{-1}$, these heterostructures exhibit a high initial specific capacity of $679.1 \text{ mA h g}^{-1}$ and a reversible capacity of $197.2 \text{ mA h g}^{-1}$ with a coulombic efficiency of 91.1% after 1000 cycles at 0.1 A g^{-1} . When the capacity was tested at 1.0 A g^{-1} , the structure delivered $192.9 \text{ mA h g}^{-1}$ after 300 cycles. Furthermore, the hollow heterostructures exhibit excellent rate performance. Therefore, this work provides an effective design of heterogeneous materials for applications in power grid energy storage systems using ZIBs in the future.

Conflicts of interest

There are no conflicts to declare.

Acknowledgements

The authors acknowledge the financial support from the Talent Introduction Start-Up Foundation of Guangxi Minzu University (2021KJQD08), the Natural Science Foundation of China (No. 22074130), the Key Scientific Research Projects of Henan Province (232102320040), the National Natural Science Foundation of China (22004032) and the Hunan Provincial Natural Science Foundation of China (2021JJ20020). The authors also acknowledge the great support from the Analysis Testing Center of Xinyang Normal University for materials characterization.

References

- 1 X. Xiao, J. Y. Yin, S. Shen, Z. Y. Che, X. Wan, S. L. Wang and J. Chen, Advances in solid-state fiber batteries for wearable bioelectronics, *Curr. Opin. Solid State Mater. Sci.*, 2022, **26**, 101042.
- 2 H. Yin, K. S. Hui, X. Zhao, S. Mei, X. Lv, K. N. Hui and J. Chen, Eco-Friendly synthesis of self-supported N-Doped Sb₂S₃-Carbon fibers with high atom utilization and zero discharge for commercial full Lithium-Ion batteries, *ACS Appl. Energy Mater.*, 2020, **3**, 6897–6906.
- 3 Q. Zhao, Q. Z. Zhu, J. W. Miao, P. Zhang, P. B. Wan, L. Z. He and B. Xu, Lithium-ion batteries: flexible 3D porous MXene foam for high-performance lithium-ion batteries, *Small*, 2019, **20**, 1970276.
- 4 X. Xiao, X. Xiao, Y. Zhou, X. Zhao, G. Chen, Z. Liu, Z. Wang, C. Lu, M. Hu, A. Nashalian, S. Shen, K. Xie, W. Yang, Y. Gong, W. Ding, P. Servati, C. Han, S. X. Dou, W. Li and J. Chen, An ultrathin rechargeable solid-state zinc ion fiber battery for electronic textiles, *Sci. Adv.*, 2021, **7**, eabl3742.
- 5 M. Y. Bao, Z. C. Y. Zhang, X. G. An, J. Liu, J. K. Feng, B. J. Xi and S. L. Xiong, Introducing Ce ions and oxygen defects into V₂O₅ nanoribbons for efficient aqueous zinc ion storage, *Nano Res.*, 2022, **16**, 2445–2453.
- 6 G. T. Zan, T. Wu, P. Hu, Y. H. Zhou, S. L. Zhao, S. M. Xu, J. Chen, Y. Cui and Q. S. Wu, An approaching-theoretical-capacity anode material for aqueous battery: Hollow hexagonal prism Bi₂O₃ assembled by nanoparticles, *Energy Storage Mater.*, 2020, **28**, 82–90.
- 7 Z. Z. C. Y. Zhang, B. J. Xi, X. Wang, X. J. Ma, W. H. Chen, J. K. Feng and S. L. Xiong, Oxygen defects engineering of VO₂·xH₂O nanosheets via *in situ* polypyrrole polymerization for efficient aqueous zinc ion storage, *Adv. Funct. Mater.*, 2021, **31**, 2103070.
- 8 H. B. Lu, Z. Z. C. Y. Zhang, X. G. An, J. K. Feng, S. L. Xiong and B. J. Xi, *In situ* electrochemically transforming VN/V₂O₃ heterostructure to highly reversible V₂NO for excellent zinc ion storage, *Small Struct.*, 2023, **4**, 2300191.
- 9 H. Q. Liu, Y. N. He, H. Zhang, K. Z. Cao, S. D. Wang, Y. Jiang, Q. S. Jing and L. F. Jiao, Lowering the voltage-hys-

teresis of CuS anode for Li-ion batteries via constructing heterostructure, *Chem. Eng. J.*, 2021, **425**, 130548.

10 J. T. Cao, Z. H. Gao, Y. L. Wang, C. Shao, S. W. Ren and Y. M. Liu, Novel Hexagonal Phase Cadmium Sulfide Nanomaterials Based Photoelectrochemical Immunosensor for Sensitive Detection of Prostate Specific Antigen, *J. Xinyang Norm. Univ., Nat. Sci. Ed.*, 2023, **153**, 535–539.

11 J. Xu, Z. Dong, K. J. Huang, L. N. Wang, Z. N. We, L. Yu and X. Wu, Flexible design of large layer spacing V-MoS₂@C cathode for high-energy zinc-ion battery storage, *Scr. Mater.*, 2022, **209**, 114368.

12 Y. Li, Z. H. Xing and H. D. Zhang, A novel electrochemical method based on layered tungsten disulfide and Au nanocomposites for the determination of bisphenol, *J. Xinyang Norm. Univ., Nat. Sci. Ed.*, 2022, **35**, 621–625.

13 H. G. Qin, Z. H. Yang, L. L. Chen, X. Chen and L. M. Wang, A high-rate aqueous rechargeable zinc ion battery based on the VS₄@rGO nanocomposite, *J. Mater. Chem. A*, 2018, **6**, 23757.

14 L. N. Wang, X. C. Tan, Q. G. Zhu, Z. Dong, X. Wu, K. J. Huang and J. Xu, The universality applications of MoS₂@MnS heterojunction hollow microspheres for univalence organic or multivalence aqueous electrolyte energy storage device, *J. Power Sources*, 2022, **518**, 230747.

15 L. X. Fang, M. D. Lan, B. Liu and Y. Cao, Synthesis and electrochemical performance of flower-like, *J. Xinyang Norm. Univ., Nat. Sci. Ed.*, 2022, **35**, 615–620.

16 M. Z. Geng, H. Q. Yang and C. Q. Shang, The multi-functional effects of CuS as modifier to fabricate efficient interlayer for Li-S batteries, *Adv. Sci.*, 2022, **9**, 2204561.

17 X. W. Zhao, Z. C. Liu, W. Y. Xiao, H. Y. Huang, L. H. Zhang, Y. H. Cheng and J. Y. Zhang, Low crystalline MoS₂ nanotubes from MoS₂ nanomasks for lithium ion battery applications, *ACS Appl. Energy Mater.*, 2020, **3**, 7580–7586.

18 K. Ma, Y. R. Dong, H. Jiang, Y. J. Hu, P. Saha and C. Z. Li, Densified MoS₂/Ti₃C₂ films with balanced porosity for ultrahigh volumetric capacity sodium-ion battery, *Chem. Eng. J.*, 2021, **413**, 127479.

19 F. E. Niu, Z. C. Bai, Y. Y. Mao, S. Q. Zhang, H. R. Yan, X. Xu, J. M. Chen and N. N. Wang, Rational design of MWCNTs @ amorphous carbon@MoS₂: Towards high performance cathode for aqueous zinc-ion batteries, *Chem. Eng. J.*, 2021, **453**, 139933.

20 S. W. Li, Y. C. Liu, X. D. Zhao, Q. Y. Shen, W. Zhao, Q. W. Tan, N. Zhang, P. Li, L. F. Jiao and X. H. Qu, Sandwich-like heterostructures of MoS₂/Graphene with enlarged interlayer spacing and enhanced hydrophilicity as high-performance cathodes for aqueous Zinc-ion batteries, *Adv. Mater.*, 2021, **33**, 2007480.

21 F. Shao, Y. F. Huang, X. L. Wang, Z. J. Li, X. D. Huang, W. T. Huang, L. B. Dong, F. Y. Kang, W. B. Liu and C. Xu, MoS₂ with high 1T phase content enables fast reversible zinc-ion storage via pseudocapacitance, *Chem. Eng. J.*, 2022, **448**, 137688.

22 S. M. Xu, X. Liang, X. Y. Wu, S. L. Zhao, J. Chen, K. X. Wang and J. S. Chen, Multistaged discharge constructing heterostructure with enhanced solid-solution behavior for long-life lithium-oxygen batteries, *Nat. Commun.*, 2019, **10**, 5810.

23 Z. H. Jin, X. B. Hu, L. J. Xu, Y. P. Xie and Z. W. Zhang, Synthesis and characterization of Co-Ni-S/MXene composite electrode materials for supercapacitor performance, *J. Xinyang Norm. Univ., Nat. Sci. Ed.*, 2023, **153**, 540–543.

24 Y. Q. Teng, H. L. Zhao, Z. J. Zhang, Z. L. Li, Q. Xia, Y. Zhang, L. N. Zhao, X. F. Du, Z. H. Du, P. P. Lv and K. Świerczek, MoS₂ nanosheets vertically grown on graphene sheets for Lithium-ion battery anodes, *ACS Nano*, 2016, **10**, 8526–8535.

25 X. Wang, Z. Z. C. Y. Zhang, M. Huang, J. K. Feng, S. L. Xiong and B. J. Xi, In situ electrochemically activated vanadium oxide cathode for advanced aqueous Zn-Ion batteries, *Nano Lett.*, 2022, **22**, 119–127.

26 H. Wang, X. Lan, D. Jiang, Y. Zhang, H. Zhong, Z. Zhang and Y. Jiang, Sodium storage and transport properties in pyrolysis synthesized MoSe₂ nanoplates for high performance sodium-ion batteries, *J. Power Sources*, 2015, **283**, 187–194.

27 L. Zeng, Y. Fang, L. Xu, C. Zheng, M.-Q. Yang, J. He, H. Xue, Q. Qian, M. Wei and Q. Chen, Rational design of few-layer MoSe₂ confined within ZnSe-C hollow porous spheres for high-performance lithium-ion and sodium-ion batteries, *Nanoscale*, 2019, **11**, 6766–6775.

28 T. S. Wang, D. Legut, Y. C. Fan, J. Qin, X. F. Li and Q. F. Zhang, Building fast diffusion channel by constructing metal sulfide/metal selenide heterostructures for high-performance sodium ion batteries anode, *Nano Lett.*, 2020, **20**, 6199–6205.

29 X. Zhang, X. Li, J. Liang, Y. Zhu and Y. Qian, Synthesis of MoS₂@C nanotubes via the kirkendall effect with enhanced electrochemical performance for lithium ion and sodium ion batteries, *Small*, 2016, **12**, 2484–2491.

30 H. Q. Liu, J. J. Fu, X. X. Wang, Y. Guo, X. Gong, Z. H. Jin and K. Z. Cao, Preparation and SERS property of PVDF self-powered flexible substrate, *J. Xinyang Norm. Univ., Nat. Sci. Ed.*, 2023, **152**, 385–389.